aerospace

MDPI

Article

Startup Characteristics and Thermal Instability of a Visual Loop Heat Pipe Under Acceleration Force

Lijun Chen [1], Yongqi Xie [1], Longzhu Han [1,*], Huifeng Kang [2] and Hongwei Wu [3,*]

[1] School of Aeronautic Science and Engineering, Beihang University, Beijing 100191, China; cljzy2305514@buaa.edu.cn (L.C.); xyq@buaa.edu.cn (Y.X.)
[2] School of Aerospace Engineering, North China Institute of Aerospace Engineering, Langfang 065000, China; huifengabc596@163.com
[3] School of Physics, Engineering and Computer Science, University of Hertfordshire, Hatfield AL10 9AB, UK
* Correspondence: hlz@buaa.edu.cn (L.H.); h.wu6@herts.ac.uk (H.W.)

Abstract

Loop heat pipes are efficiently two-phase heat transfer devices in the field of aircraft thermal management. To investigate the startup behavior and thermal instability of loop heat pipes under acceleration force, this study designed a novel loop heat pipe featuring two visual compensation chambers and a visual condenser. Elevated acceleration experiments were conducted across four different heat loads, acceleration magnitudes, and directions. The heat load ranged from 30 W to 150 W, while the acceleration magnitude varied from 1 g to 15 g, with four acceleration directions (A, B, C, and D). The startup behavior, thermal instability, internal flow pattern, and phase distribution were analyzed systematically. The experimental results reveal the following: (i) The startup behaviors vary across the four acceleration directions. In direction A, startup is more difficult due to additional resistance induced by the acceleration force. In direction C, startup time generally decreases with increasing heat load and acceleration up to 7 g. The longest startup time observed is 372 s at 30 W and 11 g. (ii) At high heat load, periodic temperature fluctuations are observed, particularly in directions B and C. Simultaneously, the vapor–liquid phase interface in the condenser exhibits periodic back-and-forth movement. (iii) The visual DCCLHP exhibits a loss of temperature control under the combined influence of high heat loads and acceleration force, often accompanied by working fluid reverse flow, periodic temperature fluctuations, or wick dry-out.

Keywords: electronic cooling; loop heat pipe; acceleration; visualization; startup; instability

check for updates

Academic Editor: Hossein Zare-Behtash

Received: 25 July 2025
Revised: 26 August 2025
Accepted: 2 September 2025
Published: 4 September 2025

Citation: Chen, L.; Xie, Y.; Han, L.; Kang, H.; Wu, H. Startup Characteristics and Thermal Instability of a Visual Loop Heat Pipe Under Acceleration Force. *Aerospace* **2025**, *12*, 797. https://doi.org/10.3390/aerospace12090797

1. Introduction

The miniaturization and integration of avionics in advanced aircraft have led to a significant increase in heat flux densities, even exceeding 500 W/cm^2 [1]. Without effective thermal management, heat accumulation in confined spaces generates localized hot spots that significantly degrade operational performance and reliability [2–4]. As a capillary-driven, phase-change heat transfer technology, the loop heat pipe (LHP) offers key advantages, including high heat transfer capacity, long-distance thermal transport, excellent temperature uniformity, and zero additional energy consumption [5–8]. These properties make LHPs highly suitable for complex onboard environments and lightweight design requirements, positioning them as an effective solution for avionics thermal management [9,10].

Successful startup is essential for the stable operation of an LHP. During the transition from startup to steady-state operation, phenomena such as temperature fluctuations and uncontrolled temperature rise may occur, directly affecting the thermal regulation performance of the LHP. Several studies have experimentally investigated the startup behavior [11–13] and thermal instability [14,15] of traditional single-compensation chamber (CC) LHPs, revealing their operational characteristics under microgravity [16,17], normal gravity [18,19], and even varying gravity conditions [20,21]. Dual compensation chamber loop heat pipes (DCCLHPs), known for their ability to accommodate varying orientations and to operate reliably in complex onboard environments [22], have attracted increasing attention. However, research on the startup and instability performance of DCCLHPs remains limited, and studies under the influence of acceleration forces are scarce. Therefore, the following literature review primarily focuses on the startup behavior, temperature fluctuations, and loss of temperature control in DCCLHPs.

In two related studies, Gerhart and Gluck and Gluck et al. [23,24] were the first to experimentally demonstrate the adaptability of DCCLHPs to various orientations. They observed reverse flow and temperature fluctuations during startup at low heat loads. Later, Lin et al. and Bai et al. [25,26] confirmed that DCCLHPs could overcome startup challenges in adverse orientations and achieve reliable startup at high heat loads. They also identified differences in startup behavior across orientations and noted temperature overshoot at low heat loads. Feng et al. [27] investigated operational instabilities in DCCLHPs, including temperature hysteresis, reverse flow, and temperature fluctuations. They identified three scenarios prone to temperature fluctuations: startup at low heat loads, steady-state operation at high heat loads, and configuration where the CC with a bayonet fitting above the evaporator. Bai et al. [28,29] designed and fabricated DCCLHPs with extended or dual bayonets to enhance startup performance at low heat loads across various installation angles. Their experiments revealed temperature fluctuations and overshoot in favorable orientations, primarily due to the presence of liquid in the vapor grooves at low heat loads. While increasing the heat load mitigated temperature overshoot, startup failure persisted in extremely adverse orientations. Yang et al. [30] experimentally investigated the startup performance of a DCCLHP featuring an eccentric ceramic wick structure across six orientations. Their results showed successful startup at a low heat load of 2 W in all orientations, with temperature overshoot depending on orientation. The overshoot magnitude exhibited an inverted “V” relationship with the heat load. Fu et al. [31] investigated the startup characteristics of a DCCLHP with dual vapor and dual condenser lines. They observed temperature overshoot and oscillations during startup at low heat loads across various orientations and noted startup failure at 100 W in adverse orientations. Subsequently, they introduced a novel DCCLHP incorporating sequential CC cooling across five typical orientations [32]. This system successfully started at heat loads from 0 to 100 W in all orientations, with startup times typically under one minute. Wang et al. [33] experimentally analyzed a DCCLHP with a heat transfer capacity of 1 kW across six orientations. Their findings showed successful startup at 50 W, though orientation-induced reductions in condensate film thickness within the condenser negatively impacted startup performance. Xie et al. and Lv et al. [34,35] systematically investigated the effects of heat load, loading mode, and acceleration magnitude/direction on DCCLHP performance. Temperature fluctuations were primarily observed at 250 W and 300 W, with periodic fluctuations occurring either in the liquid line or the entire loop, depending on the load mode. Significant fluctuations also emerged under periodic acceleration, and system overheating and failure were noted at 150 W in adverse orientations.

Visualization techniques allow for direct observation of vapor–liquid phase distribution and flow patterns within LHPs, offering valuable insights into internal flow and heat transfer mechanisms. In recent years, researchers have increasingly employed these techniques to study the operational performance of both single-CC and dual-CC LHPs [36–43].

The following references focus on using visualization methods to analyze startup behavior and unstable phenomena, such as temperature fluctuations.

Cimbala et al. and Chuang et al. [44,45] utilized neutron radiography to visualize the two-phase distribution in an LHP, while Okamoto et al. [46] applied the same technique to study liquid flow behavior and dry-out in the wick during startup. They found that liquid in the wick primarily accumulated on the lower side, with its level fluctuating in response to heat load changes. Lin et al. [47] investigated the startup performance of a DCCLHP using transparent windows, examining the effects of heat load, initial vapor–liquid distributions, and orientation. The observed phenomena included bubble formation, reverse flow, oscillatory flow, and liquid redistribution in the evaporator core, primarily attributed to radial heat leakage. Yang et al. [48] studied a visual flat-plate LHP with a vapor–liquid separation structure, identifying three startup stages: pre-boiling, boiling, and stable boiling. Their results showed that a 5 mm evaporator chamber height led to a shorter startup time compared to a 1 mm height. Wang and Wei [49] found that successful startup in a novel LHP required subcooled liquid returning to the CC and effective liquid delivery to the boiling pool by the wick. Zhao et al. [50] performed visualization experiments on the CCs of a DCCLHP for aircraft anti-icing system. It was demonstrated that the DCCLHP could successfully start up under heat loads ranging from 10 W to 180 W. Additionally, the angle of attack influenced the operating temperature and could lead to temperature fluctuations across the entire loop. Zhou and Li [51] investigated two-phase flow characteristics in the evaporator and condenser, revealing that startup time decreased with increasing heat load and that condensation flow patterns were heat-load-independent. Nishikawara et al. [52] investigated the impact of eight initial vapor–liquid distribution patterns on LHP startup performance, observing meniscus oscillations at the three-phase contact line and boiling in the CC. Zhang et al. [53] examined an LHP with a semi-cylindrical glass-sealed evaporator under varying heat loads and tilt angles, finding that temperature fluctuations closely correlated with vapor–liquid phase interface movement in the evaporator core. Liu et al. [54] investigated temperature fluctuation mechanisms in an LHP with a vapor–driven jet injector. They found that high-amplitude fluctuations resulted from intermittent liquid supply to the CC, which could be mitigated by a lower filling ratio and higher heat sink temperature. Zhang et al. [55] investigated the startup characteristics of a visual flat-plate LHP with a carbon fiber capillary wick, showing that a lower filling ratio reduced startup temperature and mitigated oscillations. Song et al. [56] observed dry-out in a silicon-based ultra-thin LHP, leading to operational failure when heat flux exceeded the critical limit. At low heat flux, bubbles and droplets coexisted in the evaporator, maintaining a dynamic balance between evaporation and condensation. Wang et al. [57] visualized operational mechanisms in a flat confined LHP under varying heat loads and sink temperatures, linking temperature fluctuations to intermittent boiling caused by restrictions at the evaporator outlet. As heat load increased, the intermittent boiling cycle initially shortened before stabilizing. Du et al. [58] investigated the effects of heat load and filling ratio on temperature fluctuations in a flat LHP, identifying fluctuations during the boiling and stabilization stages. Fluctuations of the vapor–liquid phase interface further contributed to system instability. Chang et al. [59] conducted visualization experiments on an LHP with two evaporators and one condenser, finding that oscillatory phenomena in the condenser were more pronounced under gravity-assisted and anti-gravity orientations compared to the horizontal orientation. Xie et al. [60,61] studied transient and steady-state behaviors of a DCCLHP under acceleration fields. They observed vapor–liquid phase interface fluctuations and intermittent droplet splashing in the CCs under certain conditions. Additionally, phase distribution in the condenser influenced the total pressure drop of the loop.

To the best of the authors' knowledge, the startup and instability behaviors of LHPs have been examined in previous studies through visualization experiments, which have partially elucidated the underlying mechanisms. However, the current body of visualized research is predominantly grounded in normal gravity conditions, leaving a significant knowledge gap regarding the effects of acceleration forces. This study aims to address this gap by examining the startup and instability characteristics of a visual DCCLHP subjected to acceleration forces. It provides insight into the underlying flow and heat transfer mechanisms during startup, as well as the temperature fluctuations, and loss of temperature control under acceleration effects. To achieve this, a DCCLHP with two visual CCs and a visual condenser was designed and fabricated. Experiments were conducted to analyze startup behavior and instability phenomena under varying acceleration magnitudes, directions, and heat loads. The findings enhance the understanding of DCCLHP performance in elevated acceleration fields and offer valuable technical insight for its application in avionics thermal management systems.

2. Experimental Setup

2.1. Structural Design of Visual LHP

In the current work, a visual DCCLHP was designed and fabricated. The materials and dimensions of each component are listed in Table 1. A schematic diagram of the structure and a photograph of the DCCLHP are shown in Figure 1.

Table 1. Structural parameters of the visual DCCLHP.

Components	Material	Parameter	Dimensions
Evaporator	Stainless steel 316 L	ID/OD/Length (mm)	18/20/210
Wick	Nickel	ID/OD/Length (mm)	8/18/189.5
		Pore radius (μm)	1.1
		Porosity	48.5%
		Permeability (m^2)	1.3×10^{-14}
CCs	Stainless steel 316 L	Volume (ml)	50
Condenser channel	Copper	Length/Width/Height (mm)	1000/3/3
Vapor line	Stainless steel 316 L	ID/OD/Length (mm)	2/3/300
Liquid line	Stainless steel 316 L	ID/OD/Length (mm)	2/3/380

Two visual CCs were equipped at both ends of the evaporator, with a visual condenser integrated into the system via the vapor and liquid lines. The CCs were constructed with a 1.5 mm thick 316 L stainless steel shell, each featuring two high-borosilicate glass windows (5 mm thick, 31 mm in diameter). To ensure a leak-proof seal, ethylene propylene diene monomer (EPDM) gaskets were used at the connections between the end caps, glass windows, and CC shell, secured by threaded fasteners. The bayonet extended through CC2 and penetrated the evaporator core, directing the returning liquid into the core, as illustrated in Figure 1a. The visual condenser featured a copper base plate, chosen for its high thermal conductivity, paired with high-borosilicate glass windows. A serpentine flow channel, measuring 3 mm in width, 3 mm in depth, and approximately 1000 mm in length, was milled into the base plate. Sealing grooves were machined on both sides of the channel to accommodate EPDM sealing strips, preventing cross-flow of the working fluid. The cover plate, glass, and EPDM gasket were then securely fastened to the copper base plate using bolts, as shown in Figure 1b.

In this experiment, deionized water was selected as the working fluid due to its low vapor pressure, high latent heat, non-toxicity, and easy availability [62]. Based on the designed charging system, the visual DCCLHP was filled with deionized water at volume ratios of 55%, 60%, 65%, 70%, and 75%, respectively. The steady-state operating temperature of each filling ratio was obtained by experimental measurements under a 50 W heat load in a gravity field. The lowest operating temperature of 115.0 °C was obtained at the 70% filling ratio. Therefore, the optimal working fluid filling ratio was approximately 70%.

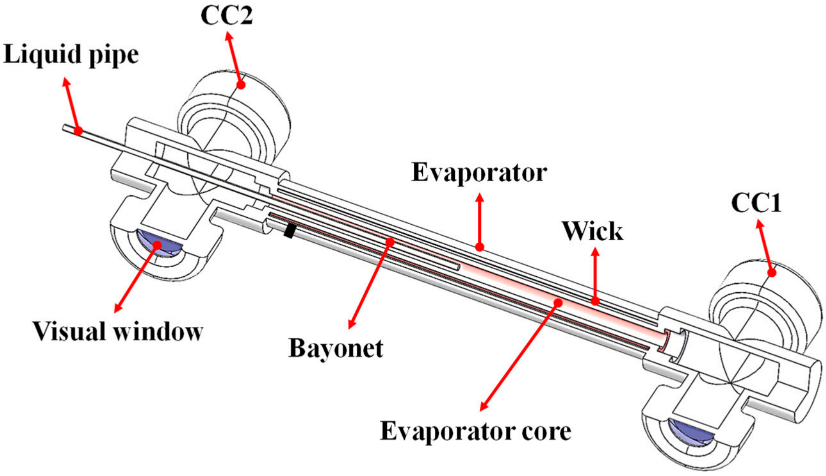

(**a**)

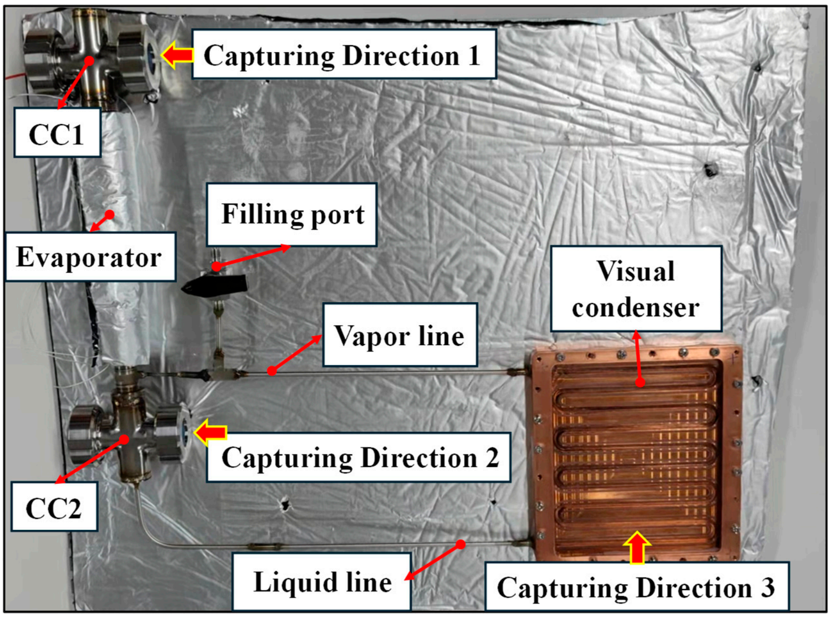

(**b**)

Figure 1. Schematic diagram of the visual DCCLHP: (**a**) structure schematic diagram of the evaporator and CCs; (**b**) photograph of the DCCLHP.

2.2. Experimental System

In this study, a visualization experimental system was developed to evaluate the operating performance of the DCCLHP under elevated acceleration conditions, as illustrated in Figure 2. The system consisted of four components: the testing unit, the refrigeration cycle system, the heat simulation and data acquisition system, and the constant acceleration simulation system.

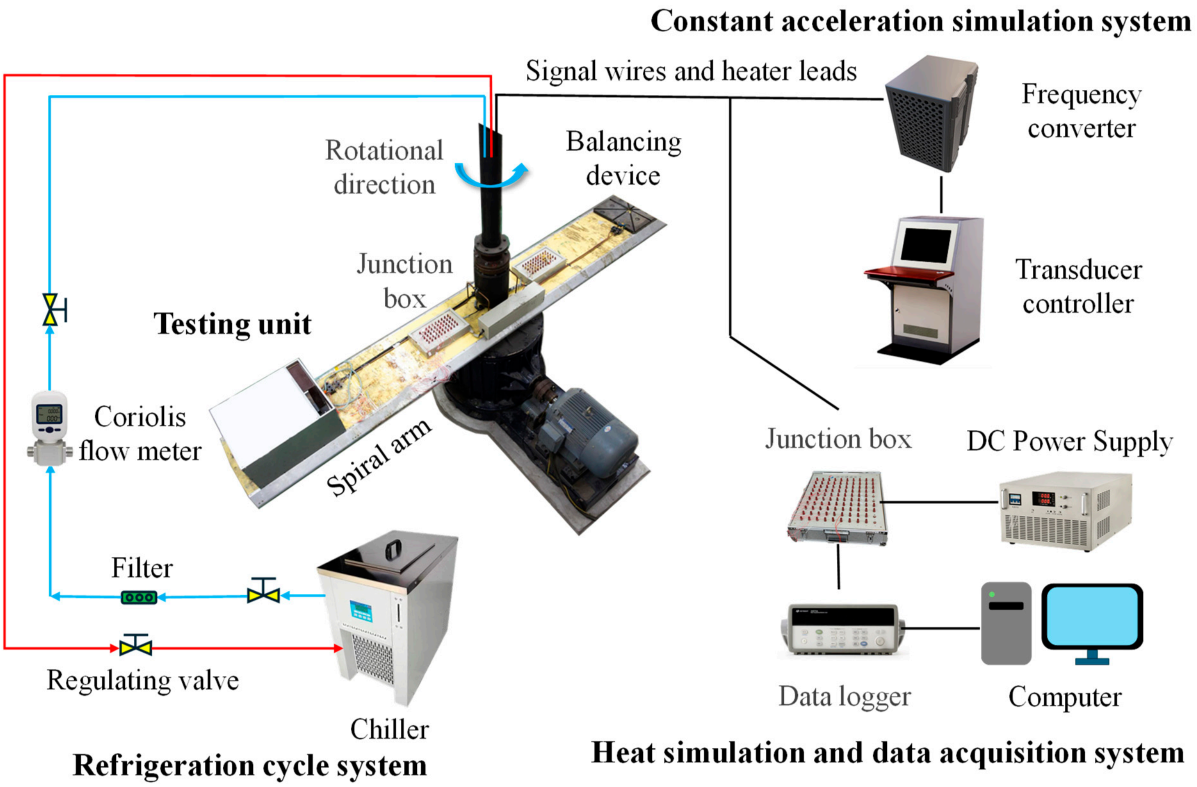

Figure 2. Schematic diagram of the experimental system.

The testing unit comprised a visual DCCLHP, three high-speed cameras (2704 × 1520 pixels, 60 fps), three LED lights, and an enclosure. The enclosure was horizontally mounted to the end of the centrifuge spiral arm using bolts, as shown in Figure 2. A water-cooling plate was positioned at the bottom of the enclosure, with the DCCLHP condenser firmly fastened to it using bolts. A layer of thermal grease was applied between the condenser and the cooling plate to reduce thermal contact resistance. The high-speed cameras were fixed near the two CCs and the condenser to capture two-phase flow behaviors within the LHP, as shown in Figure 1b. LED lights were used to ensure uniform illumination, preventing uneven exposure in the recorded images. To minimize heat exchange between the DCCLHP and the surrounding environment, all components except the visual windows were tightly wrapped with thermal insulation materials.

The refrigeration cycle system primarily consisted of a chiller (Sanffo HK-30/20 L, San Francisco, CA, USA), a filter, a water-cooling plate of 6061 aluminum, a flow meter (DMF-1, range: 0–50 kg/h, accuracy: ±0.2%), and several regulating valves. This system supplied the necessary cooling water flow rate and maintained the required temperature for the water-cooling plate. The heat simulation and data acquisition system included an electric heating film, a DC power supply (with U and I range of 0~200 V and 0~5 A, accuracies of ±0.1% and ±0.5%, respectively), multiple temperature sensors (PT100, accuracy: ±0.3 °C), a data logger (Agilent 34970A, Keysight Technologies, Santa Rosa, CA, USA), and a computer. The electric heating film was affixed to the evaporator surface, with the input power ($Q = UI$) regulated by the DC power supply to apply the heat load. The temperatures at various measurement points were recorded by the computer via the temperature sensors and the data logger. The constant acceleration simulation system comprised a rotating platform, a centrifugal acceleration simulator (Y53100-3/ZF, Xi'an Jiesheng Electronic Technology Co., Ltd., Xi'an, China), a frequency converter, and a transducer controller. The centrifuge driven by an electric motor provided up to 15 g (g = 9.81 m^2/s) rotational acceleration at the end of the spiral arm. The rotational speed of the centrifuge could be well controlled by a transducer controller with an accuracy of ±5% of the indicated speed.

2.3. Experimental Conditions

Table 2 presents the operating conditions for the visual DCCLHP experiment. However, not all heat loads and acceleration levels could be successfully tested under every acceleration direction. Considering that the centrifugal acceleration simulator used in this study had a maximum acceleration limit of 15 g, the selected acceleration levels were 1 g, 3 g, 5 g, 7 g, 9 g, 11 g, 13 g, and 15 g. Four acceleration directions were defined, which was labeled A, B, C, and D. The magnitude of the applied acceleration is determined by the rotational speed of the spiral arm of the centrifuge and the radius of the DCCLHP installed on the spiral arm. The direction of the applied acceleration is the radial acceleration direction.

Table 2. Summary of experimental conditions.

Conditions	Specific Parameters
Acceleration magnitudes ($g = 9.8\ \mathrm{m/s^2}$)	1 g\3 g\5 g\7 g\9 g\11 g\13 g\15 g
Acceleration directions	A\B\C\D
Heat load (W)	30\50\70\80\90\150
Laboratory ambient temperature (°C)	25
Cooling water inlet temperature (°C)	22

Figure 3 illustrates the relationship between the acceleration directions and the visual DCCLHP. In direction A, the condenser was located on the outer side of the spiral arm, with the acceleration aligned with the flow direction of the working fluid in the vapor line. Conversely, in direction C, the acceleration was opposite to that in direction A. In direction B, CC1 was positioned on the outer side of the spiral arm, with the acceleration parallel to the evaporator axis and directed from CC2 to CC1, whereas direction D was the reverse of direction B. Both the acceleration rotating platform and the DCCLHP were arranged horizontally. Throughout all experimental conditions, acceleration and heat load were applied simultaneously. The cooling water inlet temperature was maintained at approximately 22 °C, while the laboratory ambient temperature remained around 25 °C.

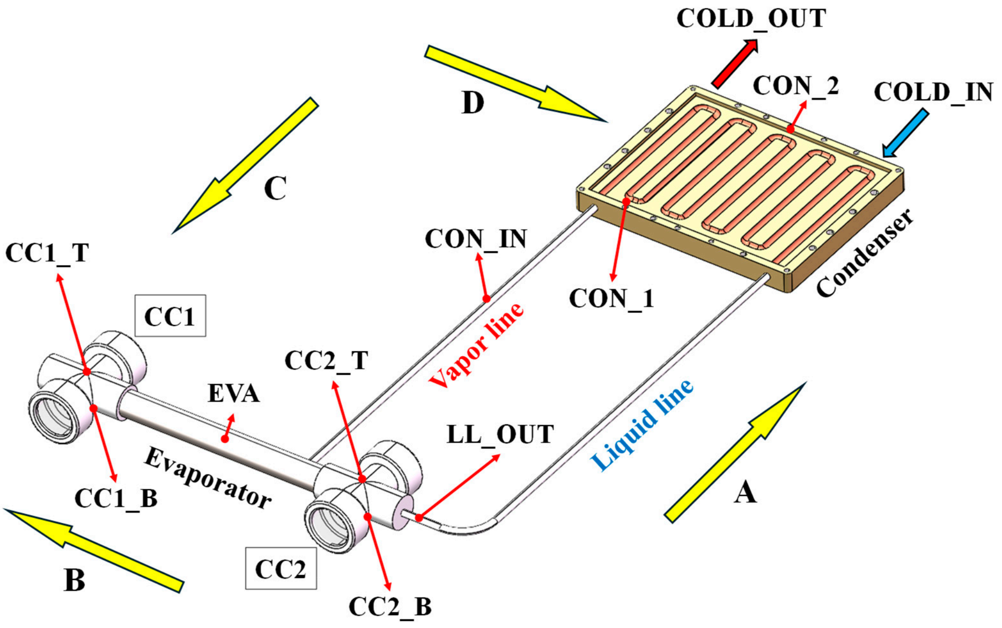

Figure 3. Schematic diagram of acceleration directions and temperature measurement point locations.

A total of eleven temperature measurement points were arranged throughout the LHP. EVA was positioned at the center of the outer surface of the evaporator to represent the evaporator temperature. COLD_IN and COLD_OUT were placed at the inlet and outlet of the water-cooling plate, respectively, to determine the average temperature of the heat sink. To monitor the two-phase state within CC1, temperature sensors CC1_T and CC1_B were installed at the top and bottom of CC1, respectively. Similarly, CC2_T and CC2_B were positioned at the top and bottom of CC2, respectively. CON_IN was positioned on the vapor line near the condenser inlet, while the LL_OUT was placed on the liquid line near CC2. Additionally, two temperature sensors, CON_1 and CON_2, were positioned on the condenser. The specific locations of these measurement points are illustrated in Figure 3.

For the directly measured variable of temperature, the measurement uncertainty was estimated to be ±0.5 °C, accounting for factors such as sensor accuracy and signal transmission distance. Given a minimum measured temperature of 15.1 °C during the experiments, the maximum uncertainty in temperature was 3.3%. Similarly, the maximum uncertainties for current and voltage were determined to be 2.63% and 0.62%, respectively. For the heat load Q, the propagated uncertainty was 2.66%.

3. Results and Discussion

3.1. Startup Behavior

3.1.1. Startup Characteristics

Figure 4 presents the temperature variations over time at different measurement points of the DCCLHP under four acceleration directions (A, B, C, and D). The corresponding heat loads and accelerations were as follows: direction A—1 g, 30 W; direction B—9 g, 70 W; direction C—1 g, 30 W; and direction D—9 g, 30 W. Additionally, Figure 5 shows the visualization results of the vapor–liquid phase distribution within the CCs for directions A and B. As depicted in Figure 4, following the application of the heat load, the evaporator temperature initially increased. After a certain period, the temperatures at the condenser inlet, CCs, and liquid line outlet began to increase. Throughout the process, the evaporator temperature remained significantly higher than that of the other components. The temperature difference between the two CCs varied depending on the acceleration directions, with relatively minor differences observed in directions A and C, whereas a more pronounced variation was evident in directions B and D. Eventually, the DCCLHP stabilized at steady-state conditions, with the corresponding evaporator temperatures reaching 91.9 °C, 117.6 °C, 84.9 °C, and 98.8 °C, for directions A, B, C, and D, respectively.

In Figure 4a, the acceleration and heat load were applied at 55 s, causing a rapid increase in the evaporator temperature. After approximately 320 s, the temperatures of CC1_T and CC2_T began to rise gradually. The reason was due to the heat transfer from the evaporator to the CCs through axial conduction. At around 430 s, the temperature at CON_IN increased abruptly, quickly reaching 26.4 °C, confirming that vapor generated in the vapor grooves had reached this measurement point. At this moment, the DCCLHP successfully started up, with a startup time of approximately 375 s and a startup temperature rise of about 44.3 °C. The visualization results under direction A in Figure 5a revealed that the centrifugal force acted on the working fluid within the CCs in a direction from the evaporator toward the condenser. Consequently, only the vapor–liquid phase interface in the CC2 was visible. It can be inferred that the vapor–liquid phase interface in both CCs was similar and exhibited a slight inclination, with liquid primarily accumulating on the side closer to the condenser. Due to the combined effects of centrifugal force and gravity, vapor predominantly accumulated at the top of the CCs. This resulted in higher temperatures at CC1_T and CC2_T, with their temperature rise rates significantly exceeding those of CC1_B and CC2_B. Upon reaching steady state, the temperatures of CC1_T and CC2_T approached that of CON_IN.

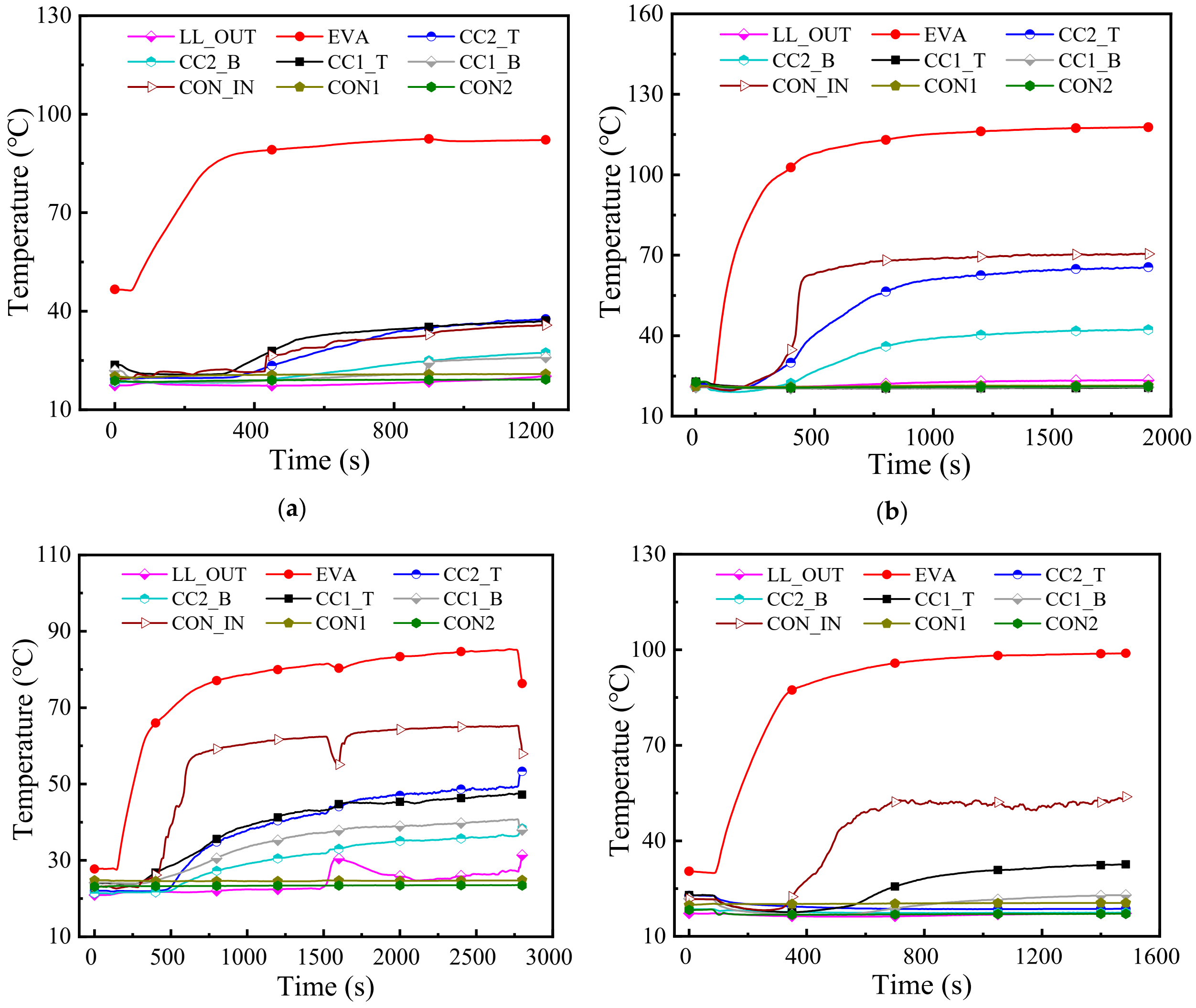

(**a**) (**b**)

(**c**) (**d**)

Figure 4. Temperature variation curves under typical operating conditions for directions A, B, C, and D: (**a**) 1 g and 30 W in direction A; (**b**) 9 g and 70 W in direction B; (**c**) 1 g and 30 W in direction C; (**d**) 9 g and 30 W in direction D.

For direction B, as shown in Figure 4b, the simultaneous application of acceleration and heat load at 80 s led to a rapid increase in the evaporator temperature. After about 250 s, the rate of temperature rise slowed and eventually stabilized. At approximately 195 s, the temperature at CON_IN began to increase, indicating that vapor generated within the vapor grooves had started entering the condenser. This marked the successful startup of the DCCLHP, with a startup time of approximately 115 s and a corresponding temperature rise of about 96.2 °C. Due to the acceleration in direction B acting from CC2 toward CC1, the CC1 region was almost entirely occupied by the liquid, while the CC2 region was predominantly filled with the vapor, as illustrated in Figure 5b. A corresponding Supplementary Materials Video S1. In the CC2, only a small portion of the liquid was located in the lower right region. Therefore, as heat was transferred from the evaporator to the CCs, the substantial heat capacity maintained both its temperature and pressure of the CC1 at relatively low levels. Consequently, the temperatures at CC1_T and CC1_B exhibited negligible variation, whereas the temperatures at CC2_T and CC2_B gradually increased.

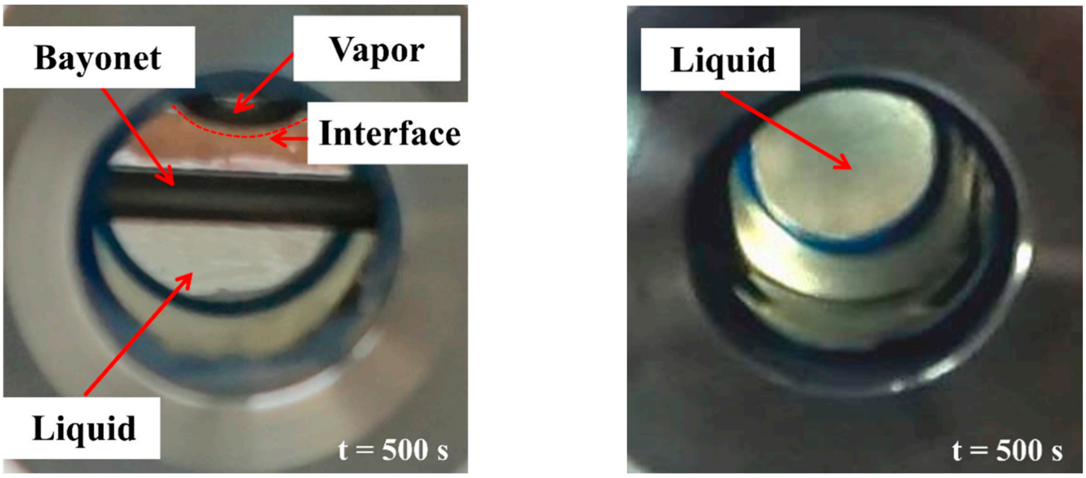

(1) CC2 t = 500 s (2) CC1 t = 500 s

(**a**)

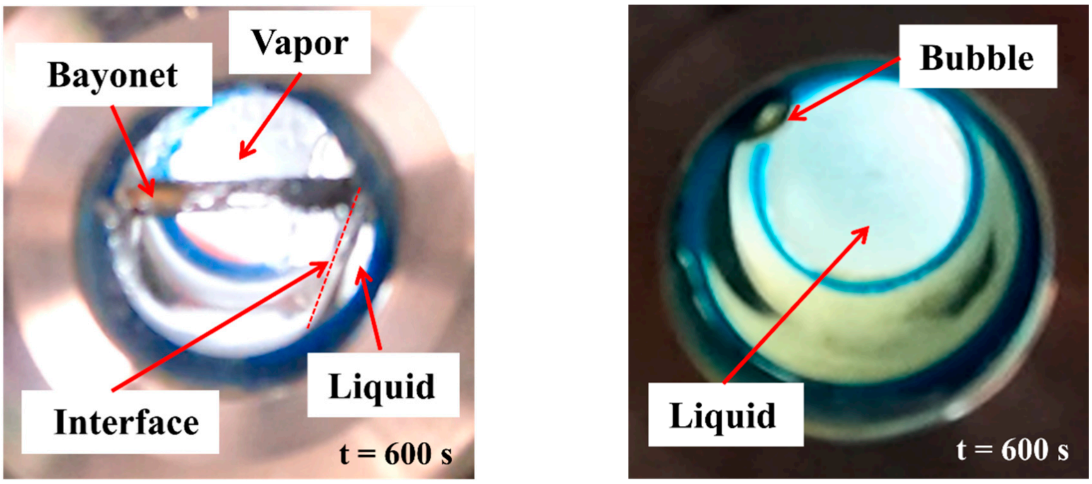

(1) CC2 t = 600 s (2) CC1 t = 600 s

(**b**)

Figure 5. Distribution of vapor–liquid working fluid within the CCs in directions A and B: (**a**) visualization results of the two CCs at 1 g and 30 W for direction A; (**b**) visualization results of the two CCs at 9 g and 70 W for direction B.

As depicted in Figure 4c, the simultaneous application of acceleration in direction C and heat load at 145 s led to a rapid increase in the evaporator temperature. After 400 s, the rate of temperature rise slowed and eventually stabilized. At 365 s, the temperature at CON_IN exhibited a sudden increase, indicating the startup of the system. The startup time was approximately 220 s, accompanied by a temperature rise of 57.5 °C. Due to the centrifugal force acting on the working fluid in the CCs under acceleration, which was opposite to that in direction A, the vapor–liquid interfaces in both CC1 and CC2 exhibited slight inclinations, with liquid primarily accumulating on the side closer to the evaporator. The acceleration in direction C facilitated the return of liquid working fluid from the condenser to the CCs. Upon startup, the temperatures of CC1_T and CC2_T gradually increased and remained relatively close to each other. Similarly, CC1_B and CC2_B exhibited a gradual temperature rise, albeit at lower values compared to CC1_T and CC2_T. The cooling effect of the returning working fluid in the bayonet on the CC2, the temperature at CC1_B was observed to be higher than that of CC2_B, with a temperature difference of 4.3 °C. At 1510 s of system operation, the temperature at LL_OUT abruptly started to increase from 22.5 °C to 30.5 °C, followed by a gradual decline after 30 s. Simultaneously, the temperature at CON_IN exhibited an opposite trend. This phenomenon could be addressed that a transient reverse flow of working fluid within the liquid line occurred, which was confirmed by the visualization result shown in Figure 6. It can be seen from Figure 6 that a large bubble entered the condenser from the liquid line, originating from the evaporator core. Fleming et al. [21] also observed a temperature rise in the liquid line caused by the reverse flow. After the system self-regulated, the working fluid promptly resumed its normal flow direction. Consequently, the LL_OUT temperature decreased while the CON_IN temperature increased to approximately 63.1 °C.

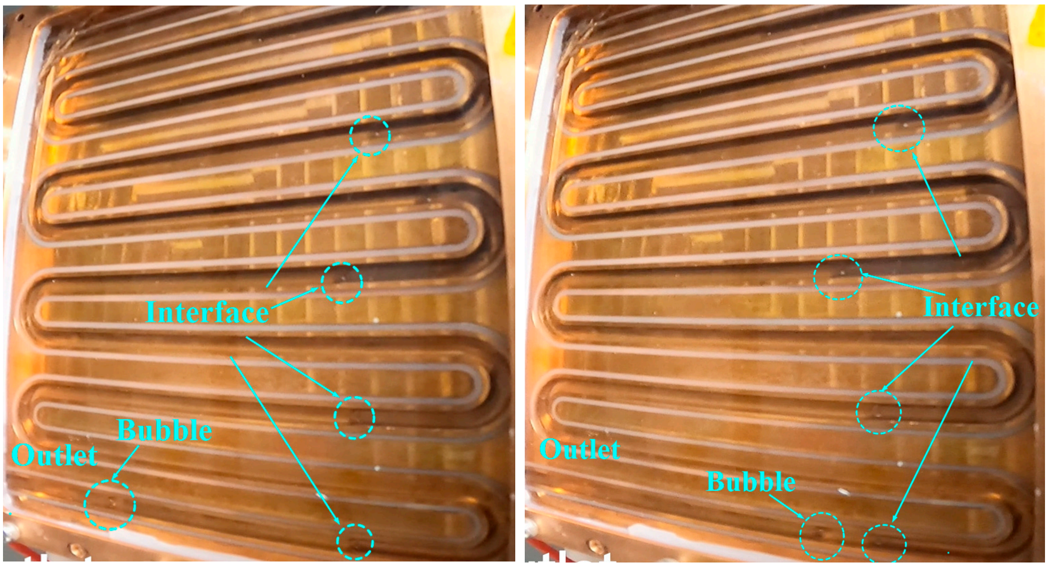

(**a**) (**b**)

Figure 6. Bubble flowing back into the condenser from the liquid line: (**a**) t = 1515 s; (**b**) t = 1518 s.

For direction D, as shown in Figure 4d, the system was activated at 315 s, with a startup time of 225 s and a startup temperature rise of 74.2 °C. Compared to direction B, the acceleration acting on the internal working fluid was directed from CC1 to CC2, resulting in an opposite vapor–liquid distribution within the two CCs. The temperature at CC1_T increased from an initial value of 22 °C to 32.5 °C, significantly higher than that of CC1_B. Since CC2 was nearly filled with liquid, the temperatures of CC2_T and CC2_B remained relatively stable, exhibiting minimal variation.

3.1.2. Startup Time

The startup time is a critical parameter for evaluating the startup performance of the LHP. A shorter startup time indicates a faster transition to steady-state operation, which is beneficial for efficient heat dissipation [63,64]. During LHP operation, the principle of mass conservation ensures that the mass flow rate remains consistent across all components. In terms of energy balance within the evaporator, the applied heat load is partially utilized for the evaporation or boiling of the working fluid in the vapor grooves, while the remainder is transferred as heat leakage to the two CCs.

In the current work, the startup time was evaluated under direction C at different heat loads and acceleration magnitudes, as shown in Figure 7. The acceleration levels were set at 1 g, 3 g, 5 g, 7 g, and 11 g, while the heat loads were 30 W, 50 W, 70 W, and 90 W. As observed in Figure 7, the startup time remained within 372 s under direction C.

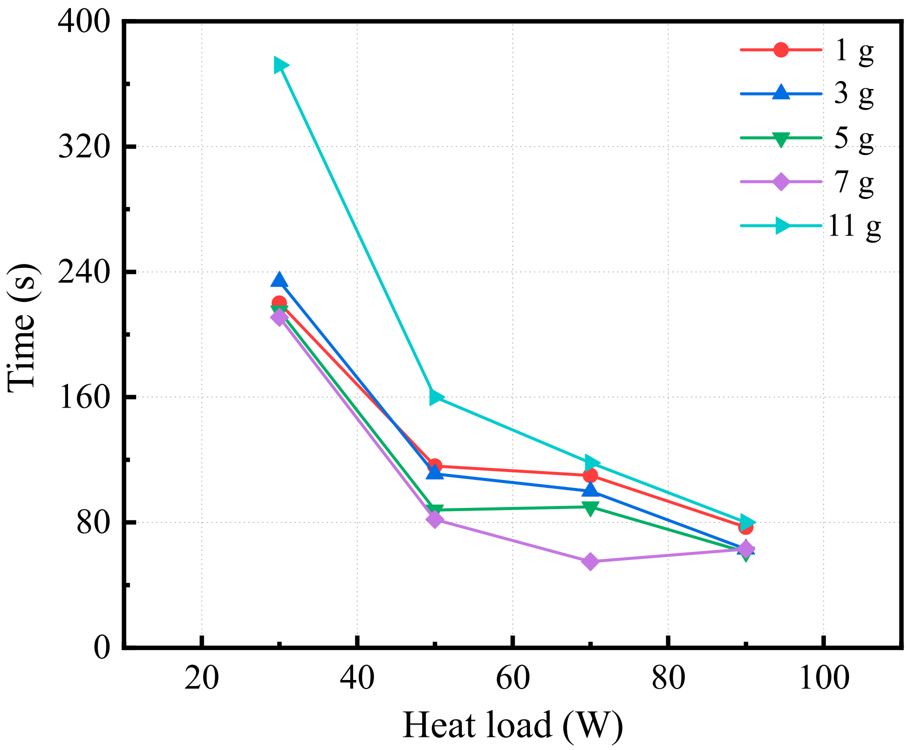

Figure 7. Startup time at different acceleration magnitudes and heat loads under direction C.

Under constant acceleration, the startup time of the DCCLHP displayed a decreasing trend as the heat load increased. Notably, when the heat load was below 70 W, the impact of heat load variation on startup time was more pronounced. At a heat load of 30 W, the startup times under accelerations of 1 g, 3 g, 5 g, 7 g, and 11 g were 220 s, 234 s, 215 s, 201 s, and 372 s, respectively. By contrast, at higher heat loads, the differences in startup time became negligible. When the heat load reached 90 W, the startup times across different accelerations converged to similar values, with startup times of 77 s, 63 s, 61 s, 63 s, and 80 s for accelerations of 1 g, 3 g, 5 g, 7 g, and 11 g, respectively. At lower heat loads, the evaporation and boiling rate of the working fluid within the vapor grooves was relatively slow. Under such operating conditions, a portion of the heat was absorbed by the liquid working fluid. Once the evaporation temperature was reached, vapor with a low flow rate entered the condenser through the vapor line. Consequently, the startup time was prolonged. Concurrently, some heat was transferred to the CCs as heat leakage, increasing their temperatures. Conversely, at higher heat loads, the evaporator temperature increased rapidly, quickly reaching the superheat required for nucleate boiling. Once vapor was generated, it facilitated system circulation and significantly reduced the startup time.

Furthermore, when the acceleration did not exceed 7 g, the startup time decreased with increasing acceleration under the same heat load. However, when the acceleration increased to 11 g, the startup time significantly increased and exceeded that of the 1 g condition. For instance, at a heat load of 30 W, the system exhibited the longest startup time of 372 s under an acceleration of 11 g, whereas the startup time was only 220 s at 1 g. This phenomenon can be explained as follows: At lower acceleration levels (1 g to 7 g), the acceleration in direction C facilitated the return of the liquid working fluid to the system, allowing for a quicker initiation of the circulating flow. As acceleration increased within this range, the startup time gradually decreased. However, at higher acceleration (above 7 g), the vapor–liquid interface in the condenser may extend into the liquid line due to the increased acceleration force, effectively reducing the length over which the acceleration acted. This resulted in a relative increase in the total flow resistance of the system. Additionally, the acceleration effect in direction C caused liquid accumulation on one side of the capillary wick within the core. For the opposite side of the wick, liquid replenishment must traverse a longer distance, while the acceleration further impeded liquid flow. Consequently, the meniscus progressively receded into the wick, leading to localized dry-out. It further caused more heat leakage from the evaporator to the CCs. This reduced the heat absorption by the liquid working fluid and slowed the phase change rate, ultimately leading to a longer startup time [51].

3.2. Temperature Fluctuation

In the current study, temperature fluctuations of the loop were also observed, primarily in directions B and C. Figure 8 presents the temperature variation curves of the DCCLHP at 11 g in direction C for heat loads of 30 W and 70 W. At 60 s, when a heat load of 30 W and an acceleration of 11 g were applied, the evaporator temperature immediately increased. At approximately 250 s, the temperatures of CC1_T and CC2_T started increasing due to a gradual increase in heat leakage from the evaporator to the CCs. Around 370 s, the temperature at CON_IN started to increase gradually. It signified the entry of vapor into the condenser and the successful startup of the DCCLHP. Upon reaching a steady state, the evaporator temperature stabilized at 81.3 °C, while both CC1_T and CC2_T remained around 32.6 °C.

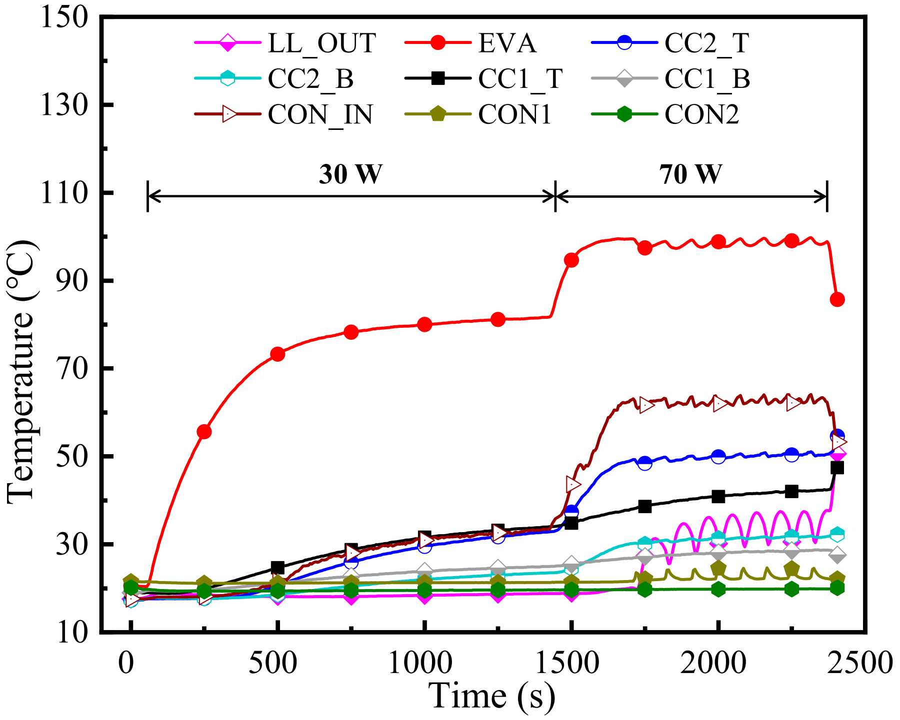

Figure 8. Temperature variation curves at 11 g and direction C for 30 W and 70 W.

When the heat load was increased to 70 W, the temperatures of the evaporator, CCs, and vapor line continued to rise. However, as the system approached a steady state, the temperatures at most measurement points began to exhibit periodic fluctuations, except for CON2 and the CC1. Among these, the temperature fluctuations at EVA, CON_IN, CON1, and LL_OUT were particularly pronounced, with fluctuations of approximately 98.5 °C, 63.0 °C, 23.1 °C, and 33.6 °C, respectively. The corresponding fluctuation amplitudes were 1.9 °C, 2.3 °C, 2.5 °C, and 7.6 °C, with a period of approximately 70 s.

Figure 9 provides images of the vapor–liquid interface positions within the condenser during temperature fluctuations in the DCCLHP. In direction C, the two-phase working fluid in the condenser was influenced by acceleration force. It caused the liquid phase to predominantly accumulate on one side of the serpentine channel, aligned with direction C, while the vapor phase was distributed on the opposite side in a segmented and intermittent pattern. The yellow dashed circles highlighted the vapor–liquid interfaces, revealing their oscillatory motion as they moved back and forth simultaneously.

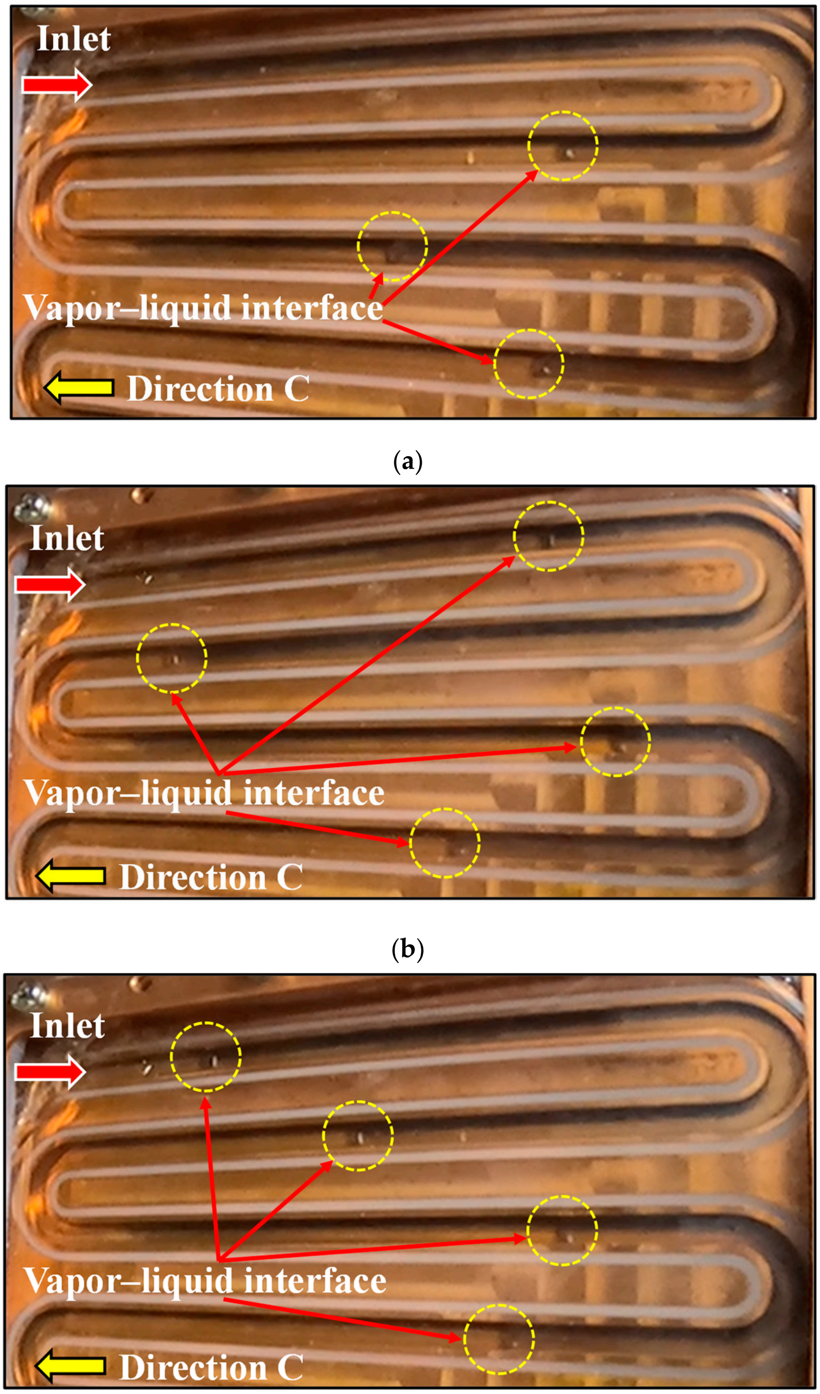

(**a**)

(**b**)

(**c**)

Figure 9. Vapor–liquid interface back and forth movement in the condenser at 11 g and 70 W for direction C: (**a**) t = 0 s; (**b**) t = 1910 s; (**c**) t = 1945 s.

This oscillatory phenomenon was closely linked to the thermodynamic re-equilibration of the system induced by acceleration force effect [52,53]. The underlying physical mechanism can be addressed as followed. Under high heat loads, the evaporator temperature increased rapidly, leading to an increased heat leakage into the CCs. Once this heat leakage reached a certain value, nucleate boiling occurred in the evaporator core, causing a sudden increase in internal temperature and pressure. This resulted in a slight backflow of the working fluid, which rapidly raised the temperature at LL_OUT and caused the vapor–liquid interface in the condenser to retreat. Consequently, the temperature at CON1 began to decrease. Simultaneously, the increase in the LL_OUT temperature reduced the subcooling of the liquid entering the CCs, disrupting the energy balance within them. This led to an increase in the temperatures of both the CCs and the evaporator. It further increased the vapor superheat in the vapor grooves and caused the temperature at CON_IN to increase. The increased vapor superheat elevated the vapor pressure, which pushed the vapor–liquid interface forward into the condenser and increased the temperature at CON1. This enhanced the subcooling of the returning working fluid with a decrease in the LL_OUT temperature. As a result, the heat leakage from the evaporator to the CCs decreased. The temperatures of the CCs and the evaporator dropped, which in turn reduced the temperature at CON_IN. Due to the time lag associated with the rise and fall of temperatures at the measurement points, a periodic oscillation was formed.

Furthermore, in direction C, the smooth return of the working fluid effectively suppressed nucleate boiling in the evaporator core, even under higher heat loads. This led to intermittent variations in the vapor–liquid interface and periodic temperature fluctuations, preventing a continuous increase in temperature. The reason of temperature fluctuations in direction B was similar to that observed in direction C.

3.3. Loss of Temperature Control

Loss of temperature control in an LHP refers to a phenomenon where the evaporator temperature continuously or rapidly rises beyond the maximum allowable operating temperature. This may occur under excessively high heat loads that exceed the heat dissipation capacity of the condenser, or under relatively low heat loads with a certain acceleration. In the current work, it should be noted that the largest heat load applied on the evaporator did not exceed the largest heat dissipation capacity of the condenser.

Figure 10 illustrates the typical loss of temperature control behaviors of the DCCLHP under acceleration directions A, B, C, and D. The corresponding acceleration and heat loads are 1 g and 90 W, 3 g and 90 W, 13 g and 150 W, and 1 g and 80 W, respectively. As shown in Figure 10, under directions A and C, the evaporator temperature exhibited a continuous rise, while under directions B and D, the evaporator temperature increased continuously with fluctuations. In all cases, the operational temperature eventually would exceed 150 °C. Considering safety concerns, the heating experiment was terminated.

In Figure 10a, upon applying the heat load at approximately 20 s, the vapor was immediately generated according to the CON_IN temperature change. Due to its low density, the vapor was less affected by the acceleration force. However, the condensed liquid working fluid experienced significant additional resistance in the liquid line and condenser due to the acceleration force, which hindered the returning flow of the liquid. As the evaporator temperature increased, the vapor pressure on the outer side of the wick also increased continuously. This led to an increase in heat leakage from the evaporator to both CCs. Consequently, a noticeable increase in the temperatures of CC1_T and CC2_T occurred after approximately 300 s. It is after approximately 630 s that an obvious increase in the LL_OUT temperature was observed. The underlying reason could be attributed to the high-temperature vapor flowing back into the liquid line. When the evaporator temperature was further raised, the vapor pressure also increased in the vapor grooves. The vapor outside the wick could penetrate into the evaporator core, leading to the pressure in the evaporator core increasing. Therefore, the vapor was driven to reversely flow into the bayonet. When the reverse vapor reached the measurement point of LL_OUT of the liquid line, the LL_OUT temperature raised. Simultaneously, the high-pressure vapor in the vapor grooves drove vapor into the condenser through the vapor line, and caused the reverse working fluid to return to the CCs. This cyclic process resulted in temperature fluctuations at the LL_OUT. Additionally, bubbles were observed passing from the condenser through the liquid line. Figure 11 shows the vapor backflow locations at 880 s and 881 s. Ultimately, the evaporator temperature exceeded 150 °C.

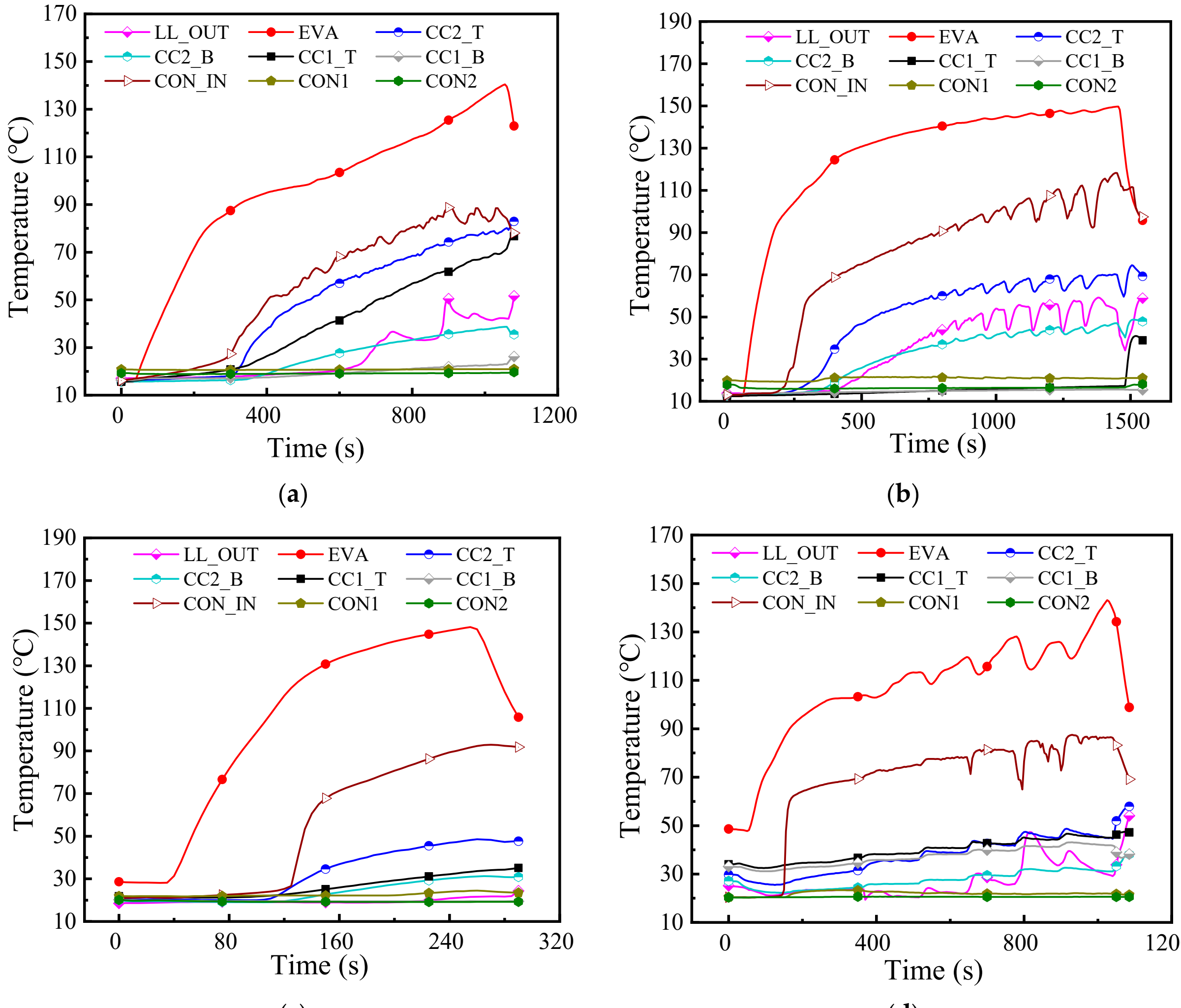

(**a**)

(**b**)

(**c**)

(**d**)

Figure 10. Loss of temperature control curves under different conditions for directions A, B, C, and D: (**a**) 1 g and 90 W in direction A; (**b**) 3 g and 90 W in direction B; (**c**) 13 g and 150 W in direction C; (**d**) 1 g and 80 W in direction D.

In Figure 10b, after applying a heat load of 90 W and an acceleration of 3 g at approximately 60 s, the evaporator temperature increased rapidly. By around 170 s, the evaporator temperature increased to approximately 90 °C, and the temperature at CON_IN began to increase. In direction B, the CC2 was primarily filled with vapor, while the CC1 mainly contained liquid. Therefore, the heat leakage from the evaporator to the CC2 caused its temperature at the CC2 to start rising at approximately 230 s. After about 320 s, the temperature at the LL_OUT also began to increase gradually. Subsequently, periodic fluctuations were observed in the temperatures of EVA, CON_IN, LL_OUT, and CC2. The temperature fluctuations at CON_IN exhibited a phase difference compared to those at LL_OUT and

CC2. Since the fluctuating temperature at LL_OUT did not exceed that of CC2_T, it could be inferred that only a portion of the high-temperature vapor backflowed into the liquid line. These observations indicate that, under a heat load of 90 W, the wick was likely to be broken down. It further led to boiling in the evaporator core and pressure fluctuations. Consequently, the system failed to maintain thermal equilibrium, which caused the amplitude of the temperature fluctuations to gradually increase. The evaporator overheated in the end.

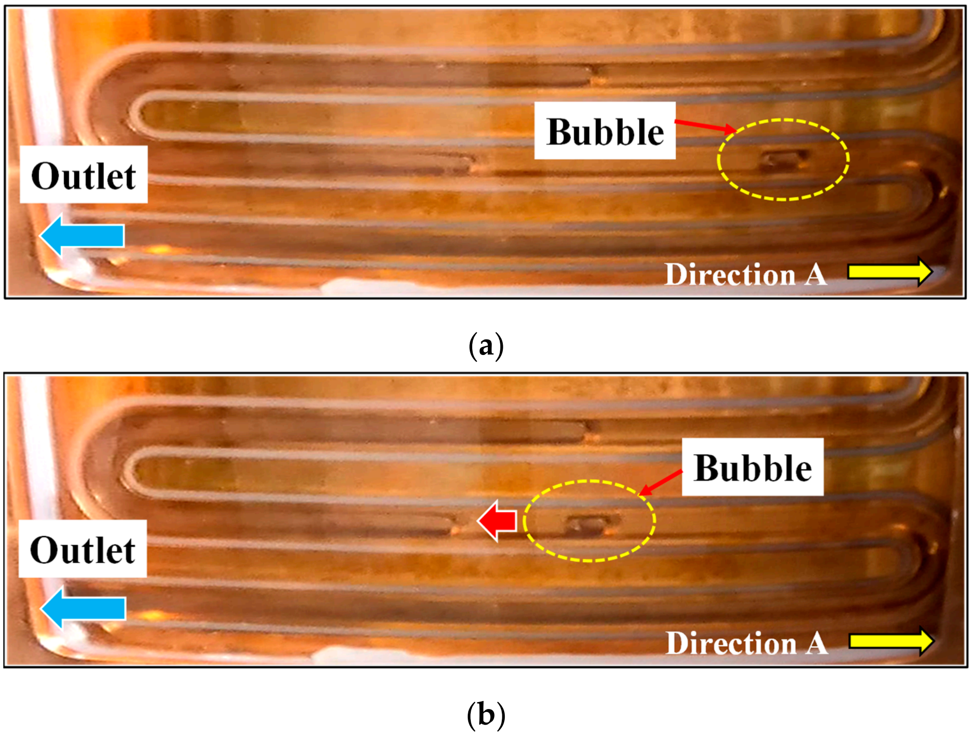

Figure 11. Vapor backflow during the loss of temperature control at 1 g and 90 W for direction A: (**a**) *t* = 880 s; (**b**) *t* = 881 s.

For the case shown in Figure 10c, the heat load reached 150 W, making it difficult for the system to establish thermal equilibrium. As a result, the evaporator temperature increased by 150 °C in just about 200 s. Although the 13 g acceleration in direction C generated a driving force that facilitated the returning flow of the liquid working fluid and reduced the operating temperature. It also made the wick more susceptible to erosion by high-temperature vapor on one side. The underlying mechanism can be explained as follows: The acceleration effect in direction C caused liquid accumulation on one side of the wick within the core, as shown in Figure 12. For the opposite side of the wick, liquid replenishment must traverse a longer distance, while the acceleration further impeded liquid flow. Consequently, the meniscus progressively receded into the wick, leading to localized dry-out. A similar dry-out of the wick was observed by Cimbala et al. [44] under a gravity field. The combined effects of the high heat load and large acceleration led to loss of temperature control in the DCCLHP.

In Figure 10d, approximately 300 s after the heat load and acceleration were applied, the evaporator began to exhibit temperature fluctuations, with the amplitude gradually increasing. Periodic temperature fluctuations were observed at CON_IN, LL_OUT, and the two CCs. In direction D, CC1 contained more vapor, while CC2 contained more liquid, with the temperature of CC1 closely aligning with that of CC2_T. Based on the temperature variations at LL_OUT, it could be inferred that the wick was likely broken down, allowing high-temperature vapor from the evaporator core to flow back into the liquid line under pressure. The combined influence of various adverse factors led to the operating temperature becoming out of control.

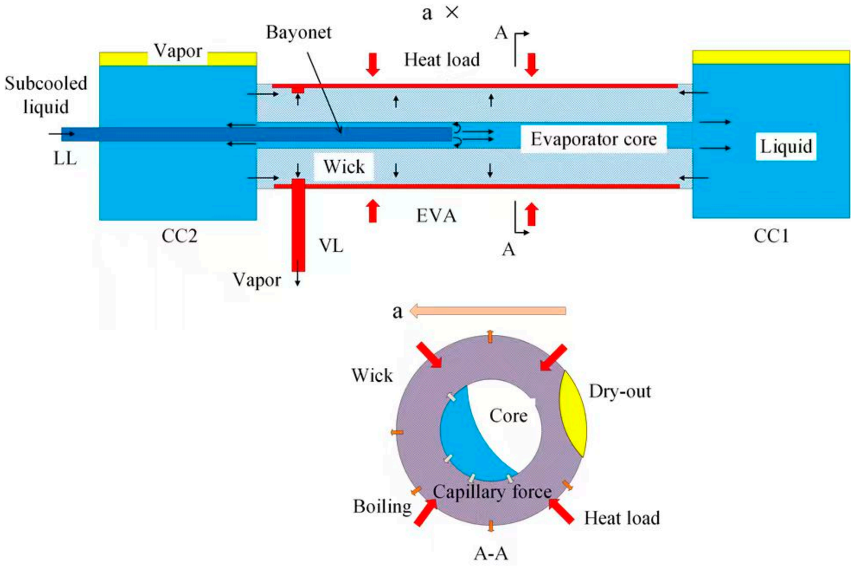

Figure 12. Speculative vapor–liquid distribution and local wick dry-out at 13 g and direction C. (The red arrow is the direction of the heat load, the black arrow is the flow direction of the working fluid, and the dark yellow and white arrows are the flow directions at the interfaces between the capillary wick and the evaporator shell, and between the evaporator core and the wick, respectively).

4. Conclusions

The current work mainly focuses on the startup performance and thermal instability of a DCCLHP with visual CCs and condenser under elevated acceleration conditions. The effects of different acceleration directions, magnitudes, and heat loads on the startup behavior are analyzed in a systematic manner. Several special instability phenomena, such as temperature fluctuations and loss of temperature control, are observed, and their underlying mechanisms are addressed. The main conclusions are as follows:

(1) The acceleration force influences the startup performance by altering the liquid distribution within the loop. Acceleration under direction A increases the flow resistance of the working fluid, resulting in longer startup times. By contrast, acceleration within the range of 1 g to 7 g under direction C reduces the startup time. However, when the acceleration under direction C increases to 11 g, the startup time reaches its maximum value of 372 s.

(2) Temperature fluctuation in the loop occurs periodically, especially at high heat loads, under directions B and C. These fluctuations are accompanied by the periodic back-and-forth movement of the vapor–liquid phase interface within the condenser, often coupled with the backflow of the working fluid into the liquid line.

(3) The visual DCCLHP exhibits a loss of temperature control under the combined influence of high heat loads and acceleration force, often accompanied by working fluid reverse flow (90 W, direction A at 1 g), periodic temperature fluctuations, or wick breakdown (90 W, direction B at 3 g).

(4) To avoid instability, such as wick dry-out and temperature fluctuations, it is recommended to reduce the wick pore size and to incorporate a secondary wick in the evaporator core. This design can improve capillary capacity to prevent vapor from penetrating into the evaporator core.

Supplementary Materials: The following supporting information can be downloaded at: https://www.mdpi.com/article/10.3390/aerospace12090797/s1, Video S1: Visualization result of CC2 at 9 g and 70 W for direction B.

Author Contributions: Conceptualization, Y.X.; Methodology, L.C. and H.W.; Formal analysis, L.C., L.H. and H.K.; Investigation, Y.X., L.H. and H.W.; Data curation, L.H.; Writing—original draft, L.C.; Visualization, H.K.; Supervision, H.W.; Project administration, Y.X.; Funding acquisition, Y.X. All authors have read and agreed to the published version of the manuscript.

Funding: The authors acknowledge financial support from the National Natural Science Foundation of China (No. 12272027).

Data Availability Statement: The original contributions presented in this study are included in the article/Supplementary Material. Further inquiries can be directed to the corresponding authors.

Conflicts of Interest: The authors declare that they have no known competing financial interests or personal relationships that could have appeared to influence the work reported in this paper.

References

1. Cui, P.; Liu, Z.; Wu, H. Subcooled flow boiling in ultrahigh-aspect-ratio microchannels for high heat flux cooling. *Int. Commun. Heat Mass Transf.* **2024**, *151*, 107221. [CrossRef]
2. Li, G.; Zhao, Y.; Zhang, X.; Xie, J.; Fang, X. An Experimental Study on the Flow Boiling Heat Transfer Characteristics of Deionized Water Under Rotational Hypergravity. *Aerospace* **2025**, *12*, 75. [CrossRef]
3. Scigliano, R.; De Simone, V.; Fusaro, R.; Ferretto, D.; Viola, N. Numerical simulation of heat pipe thermal performance for aerospace cooling system applications. *Aerospace* **2024**, *11*, 85. [CrossRef]
4. Zhao, X.; Su, L.; Jiang, J.; Deng, W.; Zhao, D. A review of working fluids and flow state effects on thermal performance of micro-channel oscillating heat pipe for aerospace heat dissipation. *Aerospace* **2023**, *10*, 179. [CrossRef]
5. Xiong, K.; Wang, S. Design, fabrication and characterization of porous ceramics secondary wick of a loop heat pipe to reduce heat leakage. *Int. Commun. Heat Mass Transf.* **2023**, *141*, 106582. [CrossRef]
6. Zhou, D.; Guo, L.; Lan, X.; Zhang, J.; Wang, X.; Du, W.; Xin, G. Fabrication and enhanced thermal performance of a self-rewetting wick of silicon-based loop heat pipe. *Int. Commun. Heat Mass Transf.* **2025**, *160*, 108378. [CrossRef]
7. Huang, J.; Chang, L.; Dong, B.; Wang, J.; Huang, H. Variable switching system for heat protection and dissipation of ultra-LEO satellites based on LHP coupled with TEC. *Aerospace* **2024**, *11*, 539. [CrossRef]
8. Xiong, K.; Chen, Y.; Zhang, W.; Wang, S. Establishment and analysis of a new steady-state operation model of loop heat pipe. *Int. Commun. Heat Mass Transf.* **2025**, *163*, 108754. [CrossRef]
9. Zilio, C.; Righetti, G.; Mancin, S.; Hodot, R.; Sarno, C.; Pomme, V.; Truffart, B. Active and passive cooling technologies for thermal management of avionics in helicopters: Loop heat pipes and mini-Vapor Cycle System. *Therm. Sci. Eng. Prog.* **2018**, *5*, 107–116. [CrossRef]
10. Wang, H.; Lin, G.; Qin, H.; Zhang, R.; Bai, L.; Guo, Y. Design and experimental validation of a high capacity loop heat pipe for avionics cooling. *Therm. Sci. Eng. Prog.* **2023**, *45*, 102139. [CrossRef]
11. Ji, X.; Wang, Y.; Xu, J.; Huang, Y. Experimental study of heat transfer and start-up of loop heat pipe with multiscale porous wicks. *Appl. Therm. Eng.* **2017**, *117*, 782–798. [CrossRef]
12. He, J.; Miao, J.; Bai, L.; Lin, G.; Zhang, H.; Wen, D. Effect of non-condensable gas on the startup of a loop heat pipe. *Appl. Therm. Eng.* **2017**, *111*, 1507–1516. [CrossRef]
13. Hendrayanto, P.A.; Fathoni, A.M.; Aliefiansyah, M.S.; Putra, N. Experimental study on Start-Up and heat transfer characteristics in loop heat pipes with dual heat sources for battery thermal management system. *Therm. Sci. Eng. Prog.* **2024**, *55*, 102980. [CrossRef]
14. Nashine, C.; Pandey, M.; Baraya, K.K. Experimental studies on the transient characteristics and start-up behaviour of a miniature loop heat pipe. *Appl. Therm. Eng.* **2025**, *259*, 124814. [CrossRef]
15. Liu, L.; Jiang, Z.; Lin, B.; Shao, B.; Li, N.; Dong, D.; Wu, Y. Effect of secondary wick on heat transfer performance of a loop heat pipe. *Int. J. Therm. Sci.* **2025**, *208*, 109488. [CrossRef]
16. Zhong, S.; Xie, R.; Li, Y.; Sun, X. Operational Characteristics of Loop Heat Pipe in Microgravity and Normal Gravity Environments. *J. Therm. Sci.* **2024**, *33*, 1394–1408. [CrossRef]
17. Yang, T.; Gao, T.; Zhao, S.; Zhang, P. Performance test of novel flat capillary pump loop heat pipe under anti-gravity and microgravity. *Microgravity Sci. Technol.* **2022**, *34*, 29. [CrossRef]

18. Tian, T.; Li, H.; Zhang, W.; Lai, Q.; Xie, Y.; Tan, J. The start-up characteristics of a novel loop heat pipe with stainless steel capillary wick. *Appl. Therm. Eng.* **2025**, *258*, 124553. [CrossRef]
19. Ku, J. Loop heat pipe startup behaviors. In Proceedings of the International Conference on Environmental Systems, Vienna, Austria, 10–14 July 2016. ICES-2016-24.
20. Ku, J.; Ottenstein, L.; Kaya, T.; Rogers, P.; Hoff, C. Testing of a loop heat pipe subjected to variable accelerating forces, Part 1: Start-up. *SAE Tech. Pap.* **2000**. [CrossRef]
21. Fleming, A.J.; Thomas, S.K.; Yerkes, K.L. Titanium-water loop heat pipe operating characteristics under standard and elevated acceleration fields. *J. Thermophys. Heat Transf.* **2010**, *24*, 184–198. [CrossRef]
22. Wang, H.; Lin, G.; Guo, Y.; Shen, X.; Zhao, W.; Bai, L. Experimental investigation on the performance of a high capacity dual compensation chamber loop heat pipe under the effect of acceleration. *Case Stud. Therm. Eng.* **2024**, *61*, 105013. [CrossRef]
23. Gerhart, C.; Gluck, D. Summary of operating characteristics of a dual compensation chamber loop heat pipe in gravity. In Proceedings of the 11th International Heat Pipe Conference, Tokyo, Japan, 12–16 September 1999.
24. Gluck, D.; Gerhart, C.; Stanley, S. Characterization of a high capacity, dual compensation chamber loop heat pipe. *AIP Conf. Proc. Am. Inst. Phys.* **1999**, *458*, 943–948.
25. Lin, G.; Zhang, H.; Shao, X.; Cao, J.; Ding, T.; Miao, J. Development and test results of a dual compensation chamber loop heat pipe. *J. Thermophys. Heat Transf.* **2006**, *20*, 825–834. [CrossRef]
26. Bai, L.; Lin, G.; Wen, D.; Feng, J. Experimental investigation of startup behaviors of a dual compensation chamber loop heat pipe with insufficient fluid inventory. *Appl. Therm. Eng.* **2009**, *29*, 1447–1456. [CrossRef]
27. Feng, J.; Lin, G.; Bai, L. Experimental investigation on operating instability of a dual compensation chamber loop heat pipe. *Sci. China Ser. E Technol. Sci.* **2009**, *52*, 2316–2322. [CrossRef]
28. Bai, L.; Tao, Y.; Guo, Y.; Lin, G. Startup characteristics of a dual compensation chamber loop heat pipe with an extended bayonet tube. *Int. J. Heat Mass Transf.* **2020**, *148*, 119066. [CrossRef]
29. Bai, L.; Fu, J.; Pang, L.; Tao, Y.; Lin, G.; Wen, D. Experimental study on a dual compensation chamber loop heat pipe with dual bayonet tubes. *Appl. Therm. Eng.* **2020**, *180*, 115821. [CrossRef]
30. Yang, P.; Yang, T.; Gao, T.; Zhao, S.; Liu, J.; Zhang, P. Experimental study on a dual compensation chamber loop heat pipe with a ceramic wick. *Appl. Therm. Eng.* **2023**, *230*, 120750. [CrossRef]
31. Fu, J.; Bai, L.; Zhang, Y.; Lin, G. Experimental study on the thermal performance of a dual compensation chamber loop heat pipe with dual vapor and condenser lines. *Therm. Sci. Eng. Prog.* **2023**, *43*, 101994. [CrossRef]
32. Fu, J.; Bai, L.; Zhang, Y.; Wang, H.; Lin, G. Improved startup performance of a dual compensation chamber loop heat pipe by sequential cooling to the compensation chambers. *Int. J. Heat Mass Transf.* **2024**, *233*, 126046. [CrossRef]
33. Wang, H.; Lin, G.; Guo, Y.; Zhao, W.; Bai, L. Experimental study of a high-capacity dual compensation chamber loop heat pipe at different orientations. *Int. J. Therm. Sci.* **2024**, *202*, 109051. [CrossRef]
34. Xie, Y.; Li, X.; Han, L.; Zhu, J.; Gao, H.; Wen, D. Experimental study on operating characteristics of a dual compensation chamber loop heat pipe in periodic acceleration fields. *Appl. Therm. Eng.* **2020**, *176*, 115419. [CrossRef]
35. Lv, X.; Xie, Y.; Zhang, H.; Xu, Y.; Wu, H.; Day, R.; Ren, J. Temperature fluctuation of a dual compensation chamber loop heat pipe under acceleration conditions. *Appl. Therm. Eng.* **2021**, *198*, 117450. [CrossRef]
36. Bartuli, E.; Vershinin, S.; Maydanik, Y. Visual and instrumental investigations of a copper–water loop heat pipe. *Int. J. Heat Mass Transf.* **2013**, *61*, 35–40. [CrossRef]
37. Yan, K.; Li, N.; Zhao, R.; Wu, Y.; Xie, R. Visualization study on the condensation in a propylene loop heat pipe operating at condenser temperatures between 153 and 283 K. *Appl. Therm. Eng.* **2021**, *185*, 116349. [CrossRef]
38. Zhao, S.C.; Zhang, Z.K.; Zhao, R.Z.; Liu, Z.C.; Liu, W. Experimental study on global visualization of loop heat pipe with a flat disk-shaped evaporator. *Energy Rep.* **2022**, *8*, 10895–10912. [CrossRef]
39. Yamada, Y.; Nishikawara, M.; Yanada, H.; Ueda, Y. Predicting the performance of a loop heat pipe considering evaporation from the meniscus at the three-phase contact line. *Therm. Sci. Eng. Prog.* **2019**, *11*, 125–132. [CrossRef]
40. Nishikawara, M.; Tomita, S.; Yokoyama, H.; Yanada, H. Relationship between phase distribution and heat-transfer coefficient of loop heat pipe evaporator investigated by lateral observation of porous media. *Appl. Therm. Eng.* **2024**, *236*, 121524. [CrossRef]
41. Chang, X.; Watanabe, N.; Nagano, H. Visualization study of a loop heat pipe with two evaporators and one condenser under gravity-assisted condition. *Int. J. Heat Mass Transf.* **2019**, *135*, 378–391. [CrossRef]
42. Chang, X.; Watanabe, N.; Nagai, H.; Nagano, H. Visualization of thermo-fluid behavior of loop heat pipe with two evaporators and one condenser under various orientations with uneven heat loads. *Int. J. Heat Mass Transf.* **2024**, *221*, 125054. [CrossRef]
43. Zhou, X.; Hua, L.; Shao, B.; Li, N.; Jiang, Z.; Lu, Y. Visualization of vapor–liquid interface and optimization in vapor grooves of loop heat pipe. *Appl. Therm. Eng.* **2025**, *267*, 125724. [CrossRef]
44. Cimbala, J.M.; Brenizer, J.S.; Chuang, A.P.Y.; Hanna, S.; Conroy, C.T.; El-Ganayni, A.A.; Riley, D.R. Study of a loop heat pipe using neutron radiography. *Appl. Radiat. Isot.* **2004**, *61*, 701–705. [CrossRef]

45. Chuang, P.Y.A.; Cimbala, J.M.; Brenizer, J.S. Experimental and analytical study of a loop heat pipe at a positive elevation using neutron radiography. *Int. J. Therm. Sci.* **2014**, *77*, 84–95. [CrossRef]
46. Okamoto, A.; Hatakenaka, R.; Murakami, M. Visualization of a loop heat pipe using neutron radiography. *Heat Pipe Sci. Technol. Int. J.* **2011**, *2*, 161–172. [CrossRef]
47. Lin, G.; Li, N.; Bai, L.; Wen, D. Experimental investigation of a dual compensation chamber loop heat pipe. *Int. J. Heat Mass Transf.* **2010**, *53*, 3231–3240. [CrossRef]
48. Yang, Y.; Zhu, K.; Wang, Y.; Wei, J.; Zheng, M.; Cui, Z. Experimental investigation and visual observation of a vapor–liquid separated flat loop heat pipe evaporator. *Appl. Therm. Eng.* **2016**, *101*, 71–78. [CrossRef]
49. Wang, X.; Wei, J. Visual investigation on startup characteristics of a novel loop heat pipe. *Appl. Therm. Eng.* **2016**, *105*, 198–208. [CrossRef]
50. Zhao, Y.; Chang, S.; Yang, B.; Zhang, W.; Leng, M. Experimental study on the thermal performance of loop heat pipe for the aircraft anti-icing system. *Int. J. Heat Mass Transf.* **2017**, *111*, 795–803. [CrossRef]
51. Zhou, G.; Li, J. Two-phase flow characteristics of a high performance loop heat pipe with flat evaporator under gravity. *Int. J. Heat Mass Transf.* **2018**, *117*, 1063–1074. [CrossRef]
52. Nishikawara, M.; Otani, K.; Ueda, Y.; Yanada, H. Liquid–vapor phase behavior and operating characteristics of the capillary evaporator of a loop heat pipe at start-up. *Int. J. Therm. Sci.* **2018**, *129*, 426–433. [CrossRef]
53. Zhang, Q.; Lin, G.; Shen, X.; Bai, L.; Wen, D. Visualization study on the heat and mass transfer in the evaporator-compensation chamber of a loop heat pipe. *Appl. Therm. Eng.* **2020**, *164*, 114472. [CrossRef]
54. Liu, L.; Yang, X.; Yuan, B.; Wei, J. Investigation of temperature fluctuations in a novel loop heat pipe with a vapor-driven jet injector. *Int. J. Heat Mass Transf.* **2021**, *179*, 121672. [CrossRef]
55. Zhang, Y.; Luan, T.; Jiang, H.; Liu, J. Visualization study on start-up characteristics of a loop heat pipe with a carbon fiber capillary wick. *Int. J. Heat Mass Transf.* **2021**, *169*, 120940. [CrossRef]
56. Song, W.; Xu, Y.; Xue, L.; Li, H.; Guo, C. Visualization experimental study on silicon-based ultra-thin loop heat pipe using deionized water as working fluid. *Micromachines* **2021**, *12*, 1080. [CrossRef]
57. Wang, X.; Yang, J.; Wen, Q.; Shittu, S.; Liu, G.; Qiu, Z.; Zhao, X.; Wang, Z. Visualization study of a flat confined loop heat pipe for electronic devices cooling. *Appl. Energy* **2022**, *322*, 119451. [CrossRef]
58. Du, S.; Zhang, Q.; Ling, L.; Zou, S.; Liu, L.; Meng, F. Visualization investigation on temperature fluctuation and two-phase behaviors of a flat loop heat pipe. *J. Therm. Sci.* **2023**, *32*, 1536–1546. [CrossRef]
59. Chang, X.; Watanabe, N.; Nagai, H.; Nagano, H. Visualization of thermo-fluid behavior of loop heat pipe with two evaporators and one condenser under various orientation with even heat loads. *Int. J. Heat Mass Transf.* **2022**, *198*, 123397. [CrossRef]
60. Xie, Y.; Fang, Z.; Zhang, H.; Wu, H.; Liu, S. Visualization study on operating performance of a dual compensation chamber loop heat pipe under acceleration condition. *Appl. Therm. Eng.* **2022**, *217*, 119157. [CrossRef]
61. Xie, Y.; Pu, W.; Liu, S.; Wu, H.; Fang, Z. Visualized experimental study on steady-state performance of a loop heat pipe under elevated acceleration fields. *Appl. Therm. Eng.* **2024**, *238*, 121984. [CrossRef]
62. Lee, S.H. Numerical study of convective heat transfer to supercritical water in rectangular ducts. *Int. Commun. Heat Mass Transf.* **2010**, *37*, 1465–1470. [CrossRef]
63. Bai, L.; Yang, Z.; Shen, X.; Guo, Y.; Lin, G.; Wen, D. Startup characteristics of an ammonia loop heat pipe with a rectangular evaporator. *Heat and Mass Transfer* **2022**, *58*, 813–831. [CrossRef]
64. He, S.; Zhou, P.; Liu, W.; Liu, Z. Experimental study on thermal performance of loop heat pipe with a composite-material evaporator for cooling of electronics. *Appl. Therm. Eng.* **2020**, *168*, 114897. [CrossRef]